Ferromagnetic Switching of Knotted Vector Fields in Liquid Crystal Colloids

Qiaoxuan Zhang,[1,2] Paul J. Ackerman,[1,3] Qingkun Liu,[1] and Ivan I. Smalyukh[1,2,3,4,5,*]
[1]Department of Physics, University of Colorado, Boulder, Colorado 80309, USA
[2]Materials Science and Engineering Program, University of Colorado, Boulder, Colorado 80309, USA
[3]Department of Electrical, Computer and Energy Engineering, University of Colorado, Boulder, Colorado 80309, USA
[4]Liquid Crystal Materials Research Center, University of Colorado, Boulder, Colorado 80309, USA
[5]Renewable and Sustainable Energy Institute, National Renewable Energy Laboratory and University of Colorado, Boulder, Colorado 80309, USA

(Received 17 May 2015; published 28 August 2015)

We experimentally realize polydomain and monodomain chiral ferromagnetic liquid crystal colloids that exhibit solitonic and knotted vector field configurations. Formed by dispersions of ferromagnetic nanoplatelets in chiral nematic liquid crystals, these colloidal ferromagnets exhibit spontaneous long-range alignment of magnetic dipole moments of individual platelets, giving rise to a continuum of the magnetization field $\mathbf{M}(\mathbf{r})$. Competing effects of surface confinement and chirality prompt spontaneous formation and enable the optical generation of localized twisted solitonic structures with double-twist tubes and torus knots of $\mathbf{M}(\mathbf{r})$, which exhibit a strong sensitivity to the direction of weak magnetic fields $\sim$1 mT. Numerical modeling, implemented through free energy minimization to arrive at a field-dependent three-dimensional $\mathbf{M}(\mathbf{r})$, shows a good agreement with experiments and provides insights into the torus knot topology of observed field configurations and the corresponding physical underpinnings.

DOI: 10.1103/PhysRevLett.115.097802 PACS numbers: 61.30.-v, 61.30.Jf, 75.50.Dd, 02.10.Kn

Envisaged by Gauss, Kelvin, and Tait, static links and knots of looped physical field lines are now experimentally realized [1–5]. Liquid crystals (LCs) permit knotting of singular linear vortices along which molecular ordering vanishes [2,3] and also three-dimensional (3D) nonsingular topological solitons with knots and links in the molecular alignment field $\mathbf{n}(\mathbf{r}) \equiv -\mathbf{n}(\mathbf{r})$, which are labeled by elements of the third homotopy group $\pi_3(\mathbf{R}P^2) = \mathbf{Z}$ [1,4,5]. However, their $\pi_3(\mathbf{S}^2) = \mathbf{Z}$ counterparts in vector fields, such as the magnetization field $\mathbf{M}(\mathbf{r})$, have not been experimentally realized. Such solitons are commonly unstable according to the Hobart-Derrick theorem [6], but can arise in theoretical models with higher-order spatial derivatives (Skyrme stabilization mechanism [7]). In chiral condensed matter, such as noncentrosymmetric magnets [8,9] and cholesteric LCs [1,4,5,10,11], solitons arise as mesoscopic objects due to the system's tendency to form twisted states. For example, this enables isolated $\pi_2(\mathbf{S}^2) = \mathbf{Z}$ solitons [12] and their condensates [13] in chiral ferromagnets with potential applications in spintronics [14], as well as isolated $\pi_2(\mathbf{R}P^2) = \mathbf{Z}$ and $\pi_3(\mathbf{R}P^2) = \mathbf{Z}$ solitons [4,11] and their self-assemblies along with other defects in chiral LCs [1,5,11].

We experimentally realize chiral ferromagnetic LC colloids (CFLCCs) with ordered ferromagnetic nanoplatelets [15] in a chiral LC host and with a spatially modulated, twisted ground-state $\mathbf{M}(\mathbf{r})$. Competition of the medium's chirality with the strong surface anchoring at bounding substrates suppresses realization of unidirectional twist in CFLCCs and prompts spontaneous or laser-guided formation of localized twisted solitonic structures with double-twist tubes and torus knots of $\mathbf{M}(\mathbf{r})$. These 3D torus knots of $\mathbf{M}(\mathbf{r})$ exhibit a strong polar response to weak magnetic fields and are accompanied by hyperbolic point defects, forming localized field configurations dubbed "torons" [1]. Numerical free energy minimization yields 3D $\mathbf{M}(\mathbf{r})$ structures matching their experimental counterparts and reveals topologically protected particlelike configurations with knotted fields that resemble the famous mathematical Hopf and Seifert fibrations [16].

Barium hexaferrite $BaFe_{11}CrO_{19}$ ferromagnetic nanoplatelets of thickness 10 nm and diameter 105 nm were synthesized by the thermohydrodrate method [17]. They are magnetically monodomain with magnetic moments ($\approx 9 \times 10^{-18}$ A m^2) orthogonal to large-area faces. The platelets were surface functionalized by 5 kDa silane-terminated polyethylene glycol (JemKem Technology) to improve stability and define homeotropic boundary conditions for $\mathbf{n}(\mathbf{r})$ in the LC. To prepare the CFLCCs, 15 μl of pentylcyanobiphenyl (5CB) was mixed with 15 μl of ethanol, and then with 15 μl of a 0.5–1 wt% magnetic platelet dispersion in ethanol, followed by ethanol evaporation maintained at 90° C for 3 h. Then, the sample was rapidly cooled to the nematic phase of 5CB while vigorously stirring. The dispersion was doped with a left-handed chiral agent cholesteryl nonanoate (Sigma-Aldrich) to yield a CFLCC pitch $p = 1/(hC_{\mathrm{CN}})$, the distance over which $\mathbf{M}(\mathbf{r}) \| \mathbf{n}(\mathbf{r})$ in the equilibrium state rotates by 360°, where $h = 6.25$ μm^{-1} is the helical twisting power and C_{CN} is the concentration of cholesteryl nonanoate (CN). The final concentration of platelets in the LC was varied within 0.05–0.1 wt%. The nanoplatelets exhibited

spontaneous alignment with the large-area faces orthogonal to $\mathbf{n}(\mathbf{r})$ and the magnetic moments along $\mathbf{n}(\mathbf{r})$, as confirmed by measuring polarization-dependent absorbance in the planar cells [Fig. 1(a)] and probing the response to the magnetic fields. Dispersions of ferromagnetic platelets in 5CB were stable at the fields $\mu_0\mathbf{H}$ up to 20 mT used in our study, exhibiting a facile response to ~1 mT.

Homeotropic cells with polydomain CFLCCs, with $\mathbf{M}(\mathbf{r})$ pointing along one of the two antiparallel directions along the vertical far-field director $\mathbf{n_0}$, were prepared using 1 or 0.17 mm thick glass plates treated with an aqueous solution of 0.1 wt% *N*, *N*-dimethyl-*N*-octadecyl-3-aminopropyl-trimethoxysilyl chloride (Acros Organics) to set perpendicular boundary conditions for $\mathbf{n}(\mathbf{r})$. Alternatively, polyamide SE1211 (Nissan Chemicals) alignment layers were prepared via spin coating and baking at 185 °C for 1 h. To define monodomain CFLCCs with only one orientation of the far-field magnetization vector $\mathbf{M_0}$, 0.5 wt% of $BaFe_{11}CrO_{19}$ nanoplatelets was added to the polyamide and spin coated in the presence of an ≈40 mT field normal to the glass plate. Ensuring the like orientation of easy axes for $\mathbf{M_0}$ at the inner surfaces of the confining plates, we defined square-inch ferromagnetic CFLCC monodomains. The cell thickness ≈60 μm was set using an UV-curable optical adhesive (NOA-65, Norland Products) containing 60 μm silica spacers. The CFLCC pitch $p \approx 70$ μm was defined using $C_{CN} = 0.23$ wt%. We probed the CFLCCs (Fig. 1) using an alternating gradient magnetometer (MicroMag 2900, Princeton Measurement Corp.) and a vibrating sample magnetometer (PPMS 6000, Quantum Design). The threshold field at which the magnetization

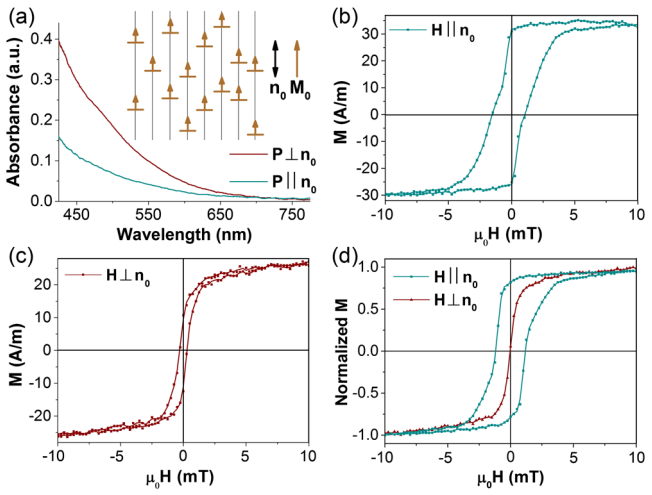

FIG. 1 (color online). Characterization of CFLCCs. (a) Optical absorbance at light polarizations $\mathbf{P}\|\mathbf{n_0}$ and $\mathbf{P}\perp\mathbf{n_0}$ for a 60 μm thick planar cell with ferromagnetic platelets at 1.6 wt% in 5CB, as schematically shown in the inset. (b),(c) Magnetic hysteresis loops for the monodomain CFLCC containing solitonic structures with (b) $\mathbf{H}\|\mathbf{n_0}$ and (c) $\mathbf{H}\perp\mathbf{n_0}$. (d) Similar data for a monodomain nonchiral ferromagnetic platelet dispersion in 5CB. The concentration of platelets in panels (b)–(d) is ≈0.1 wt%.

reversal starts for ferromagnetic colloids in a nematic host is ≈1 mT [Fig. 1(d)], whereas that of CFLCC with the same concentration (0.1 wt%) of nanoparticles is ≈0.5 mT [Fig. 1(b)]. This lower threshold for CFLCC arises due to the reduction of the elastic free energy of a field-distorted state with twist deformations and is similar to that in homeotropic cells of chiral LCs relative to their nonchiral counterparts [1]. Unlike nonchiral nematic dispersions of the same platelets in 5CB [Fig. 1(d)], which exhibit a ferromagnetic response at $\mathbf{H}\|\mathbf{n_0}$ and a paramagneticlike response at $\mathbf{H}\perp\mathbf{n_0}$, CFLCCs with solitonic structures show hysteresis loops at both $\mathbf{H}\|\mathbf{n_0}$ and $\mathbf{H}\perp\mathbf{n_0}$ [Figs. 1(b) and 1(c)].

Laser generation of solitonic structures was done using a 100 mW, 1064 nm beam from a holographic optical tweezers setup, which was focused into a CFLCC cell by a 100× objective with a numerical aperture of 1.4 [1,18]. Three-dimensional imaging of $\mathbf{n}(\mathbf{r})\|\mathbf{M}(\mathbf{r})$ utilized three-photon excitation fluorescence polarizing microscopy based on the fluorescence of 5CB molecules arising from three-photon absorption of 780 nm femtosecond light, as described elsewhere [4,5]. Implemented using an IX81 inverted microscope, this 3D imaging was utilized in combination with conventional polarizing microscopy to probe the topology and switching of the solitonic structures.

CFLCC cells with vertical surface boundary conditions for $\mathbf{n_0}$ without selection of one of the two antiparallel $\mathbf{M}\|\mathbf{n_0}$ orientations are polydomain in nature [Figs. 2(a)–2(f)] with regions of opposite $\mathbf{M}$ separated by wall defects "invisible" before [Fig. 2(a)] and apparent after applying the fields [Figs. 2(c)–2(f)]. The lateral dimensions of these domains are 2–10 times the cell thickness. In the monodomain samples [Figs. 2(g) and 2(h)], magnetization alignment layers define the same $\mathbf{M_0}$ within an inch-wide cell, showing no response to $\mathbf{H}\|\mathbf{M_0}$ and facile spatially uniform switching at other $\mathbf{H}$ orientations, including antiparallel to $\mathbf{M_0}$. Similar to chiral LCs without dispersed platelets [1,4,5,11,19], CFLCCs can host laser-generated or naturally occurring solitonic structures, which in polydomain samples can be embedded within single or multiple domains. Since such solitons are ~1000 times larger than nanoplatelets, mechanical coupling through surface boundary conditions forces platelets to orient orthogonally to $\mathbf{n}(\mathbf{r})$ and with their magnetic dipoles along $\mathbf{n}(\mathbf{r})$ [inset of Fig. 1(a)] [15], so that the spatially varying $\mathbf{M}(\mathbf{r})$ is continuous and follows the director everywhere.

Consistent with the 3D nonlinear optical imaging of $\mathbf{n}(\mathbf{r})$, similar to that reported elsewhere [4,5], numerical models of $\mathbf{M}(\mathbf{r})\|\mathbf{n}(\mathbf{r})$ reveal torons with a knotted solitonic $\mathbf{M}(\mathbf{r})$ accompanied by point defects (Fig. 3). A midplane cross section of the 3D structure shows a 2π twist of $\mathbf{M}(\mathbf{r})$ in all radial directions [Fig. 3(a)]. By numerically following the $\mathbf{M}(\mathbf{r})$ field lines from a representative set of points of this cross-sectional plane [20], corresponding to a circle marked on $\mathbf{S}^2$ in the inset of Fig. 3(d), we find that $\mathbf{M}(\mathbf{r})$ forms closed loops, all of which are linked with each other once and define a torus [Fig. 3(b)], as in the

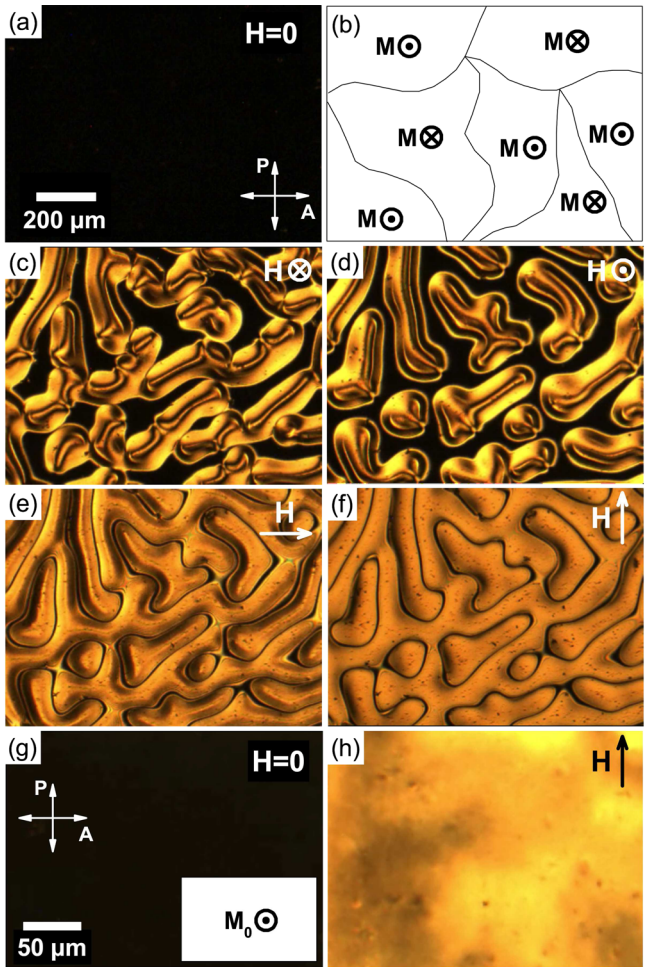

FIG. 2 (color online). Polydomain and monodomain confined CFLCCs with $p \approx 70\ \mu$m in homeotropic cells of thickness $\approx 60\ \mu$m. (a) A polarizing optical micrograph of a polydomain cell at no fields. (b) A schematic of this polydomain cell. (c)–(f) Polarizing micrographs of the same cell area as shown in (a) but for (c),(d) vertical and (e),(f) in-plane $\mathbf{H}$. (g),(h) Polarizing optical micrographs of a monodomain CFLCC (g) at no fields (remains unchanged for $\mathbf{H} \| \mathbf{M_0}$) and (h) at $\mathbf{H}$ along the arrow. The insert in (g) schematically shows a single magnetic domain of the cell. The field is ≈ 6 mT and the platelet concentration is ≈ 0.05 wt%.

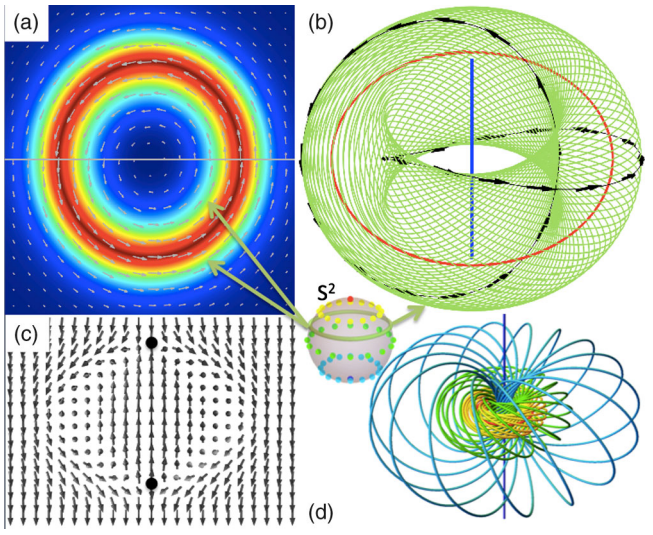

FIG. 3 (color online). CFLCC toron with a torus knot field configuration. (a) An in-plane cross section of a toron passing through the cell midplane, with colors and arrows showing $\mathbf{M}(\mathbf{r})$ orientations. (b) A torus formed by a dense series of interlinked closed loops of $\mathbf{M}(\mathbf{r})$ intersecting the cross section (a) in regions of the same $\mathbf{M}(\mathbf{r})$ orientation and color; two of these loops are decorated by arrows. $\mathbf{M}(\mathbf{r})$ along the central straight and circular axes of the double-twist torus are shown in blue and red, respectively, corresponding to the colors in (a). (c) A vertical cross section of the toron along a horizontal line in (a), with black circles marking hyperbolic point defects. (d) Hopf fibration representing the topology of $\mathbf{M}(\mathbf{r})$ in the central part of the CFLCC toron, with the color of the fibers corresponding to points on $\mathbf{S}^2$ (inset) and correlated to that of $\mathbf{M}(\mathbf{r})$ panels (a) and (b), albeit the toron's point singularities interrupt the $\mathbf{M}(\mathbf{r})$ lines emanating from the central blue-colored region of (a).

mathematical Hopf fibration and field configurations of "hopfions" [4,5]. At confining surfaces, unlike in the Hopf fibration [Fig. 3(d)], two hyperbolic point defects interrupt some of the $\mathbf{M}(\mathbf{r})$ lines, such as the ones along the toron's vertical axis [Fig. 3(c)]. These point singularities are similar to the ones in $\mathbf{n}(\mathbf{r})$ of torons in chiral nematics [1] and help to match $\mathbf{M}(\mathbf{r})$ of the toron's interior with the orientation of $\mathbf{M_0}$ [Fig. 3(c)].

CFLCC torons and solitons exhibit a facile orientation-dependent response to magnetic fields (Figs. 4 and 5), consistent with the presence of the term $-\mu_0 \int [\mathbf{M} \cdot \mathbf{H}] dV$ in the free energy functional [15,20]. In both the monodomain and polydomain samples, the lateral dimensions of the topological torons increase when $\mathbf{H}$ is along the vertical $\mathbf{M}(\mathbf{r})$ in the toron center and antiparallel to $\mathbf{M}(\mathbf{r})$ around its exterior [Figs. 4(a) and 4(b)]. Torons in monodomain CFLCCs [Fig. 4(d)] and the ones embedded in large domains of polydomain samples shrink when $\mathbf{H}$ is reversed, until they eventually disappear [Figs. 4(e) and 4(f)]. However, some torons in polydomain CFLCCs exhibit a more complex behavior for $\mathbf{H}$ antiparallel to $\mathbf{M}(\mathbf{r})$ in their interior [Fig. 4(c)], shrinking in size for some time and then laterally shifting to a nearby domain of opposite background magnetization and expanding similar to torons in domains with $\mathbf{H}$ along the vertical $\mathbf{M}(\mathbf{r})$ in the toron center [20]. This relatively slow response is present well below the threshold for realignment of monodmain CFLCCs with $\mathbf{M_0}$ antiparallel to $\mathbf{H}$ in similar cells (Fig. 1), because of the distorted $\mathbf{M}(\mathbf{r})$ (Fig. 4). Upon turning $\mathbf{H}$ off, expanded or contracted torons relax to their initial size [Figs. 4(a)–4(d)], unless $\mathbf{H}$ antiparallel to $\mathbf{M}(\mathbf{r})$ in the toron interior exceeds a certain critical value (dependent on the nanoplatelet concentration), at which the shrinking torons abruptly and irreversibly disappear. The lateral size of the torons cannot shrink below $\approx 50\%$ of its equilibrium value

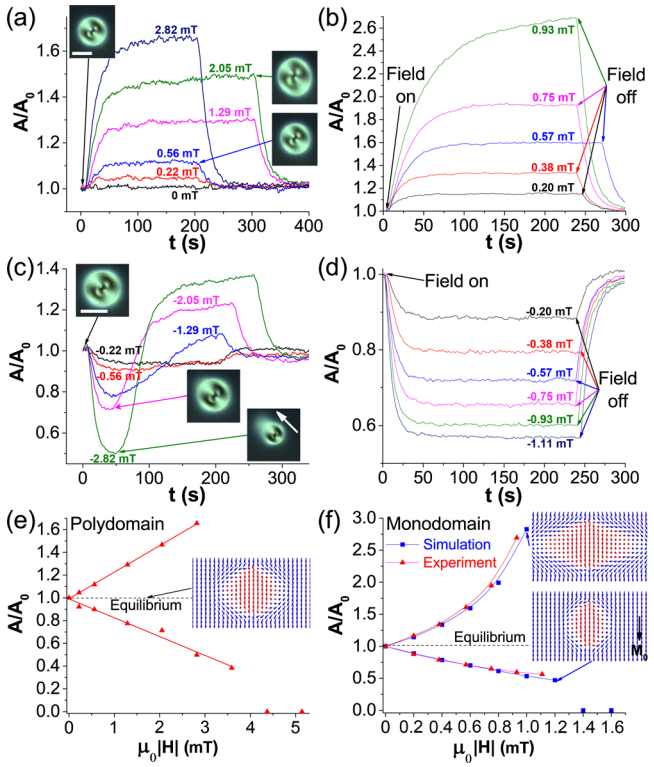

FIG. 4 (color online). Ferromagnetic switching of torons. (a),(b) Relative lateral toron area A/A_0 versus time in (a) polydomain and (b) monodomain CFLCCs for $\mathbf{H}$ along $\mathbf{M}(\mathbf{r})$ in the toron center, obtained experimentally. Insets in (a) show corresponding polarizing micrographs; the white scale bar in the top-left inset is 50 μm. (c),(d) A/A_0 versus time for $\mathbf{H}$ antiparallel to $\mathbf{M}(\mathbf{r})$ in the toron center and parallel to that of its exterior for (c) polydomain and (d) monodomain samples. $\mathbf{H}$ is turned on and off at times indicated by arrows in panels (b) and (d). In a polydomain cell (c), at a constant $\mathbf{H}$, the toron first shrinks and then expands while laterally shifting (along the white arrow in the bottom-right insert) to self-embed in a domain with a background $\mathbf{M}$ opposite to that of original domain. (e),(f) A/A_0 versus $|\mathbf{H}|$ for two opposite vertical field orientations in (e) polydomain and (f) monodomain CFLCCs. $\mathbf{H}$ is along and antiparallel to $\mathbf{M}(\mathbf{r})$ in the toron center for $A > A_0$ and $A < A_0$, respectively. Concentrations of magnetic particles in both cases are ≈0.05 wt%.

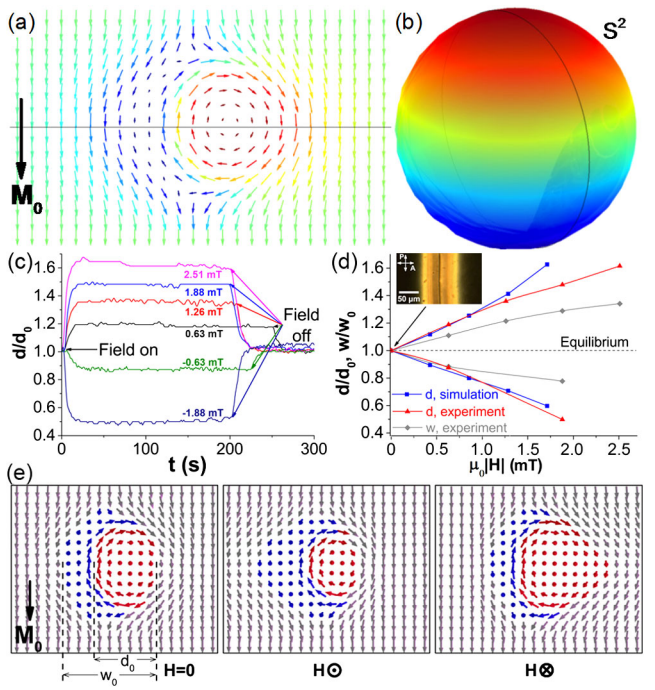

FIG. 5 (color online). Ferromagnetic switching of 2D solitons. (a) A translationally invariant solitonic $\mathbf{M}(\mathbf{r})$ shown using arrows. (b) The corresponding $\mathbf{S}^2$ order parameter space, with colors depicting vector orientations correlated with (a); the circle corresponds to the continuous $\mathbf{M}(\mathbf{r})$ rotation along the black line in (a). (c) Experimental relative change of diameter d/d_0 of a double-twist tube versus time at different $\mathbf{H}$ along $\mathbf{M}(\mathbf{r})$ on the tube axis (positive H marked on the plot) and at $\mathbf{H}$ antiparallel to $\mathbf{M}(\mathbf{r})$ on the tube axis (negative H). (d) Relative change of the overall width w/w_0 of the translationally invariant 2D soliton and diameter d/d_0 of the double-twist tube within it versus $|\mathbf{H}|$. $\mathbf{H}$ along and antiparallel to $\mathbf{M}(\mathbf{r})$ on the double-twist tube axis yields $w > w_0$ (and $d > d_0$) and $w < w_0$ (and $d < d_0$), respectively. Numerical simulations of $\mathbf{M}(\mathbf{r})$ are calibrated using experiments. (e) Computer-simulated cross sections of the 2D soliton at no fields (left) and for $\mathbf{H}$ pointing into the screen (middle) and out of the screen (right). The concentration of platelets is ≈0.05 wt%.

at $\mathbf{H} = 0$, at which a discontinuous reconfiguration of $\mathbf{M}(\mathbf{r})$ [Figs. 4(e) and 4(f)] from the initial knotted or linked to a uniform field state occurs. This type of switching is a salient feature of the topology-protected torus knot of $\mathbf{M}(\mathbf{r})$ within the toron (Fig. 3).

Our translationally invariant CFLCC solitons resemble both cholesteric fingers of the second kind [11,19] and 2D skyrmions in epitaxial MnSi thin films [21] [Figs. 5(a) and 5(b)]. The soliton contains a double-twist tube accompanied by a nonsingular bimeronlike structure [21] [Fig. 5(a)]. The projection of $\mathbf{M}(\mathbf{r})$ from this cross section onto the order parameter space, an $\mathbf{S}^2$ sphere, covers it once [Fig. 5(b)]. Switching of 2D solitons is also orientation dependent [Figs. 5(c)–5(e)]. Their double-twist tube expands when $\mathbf{H}$ matches $\mathbf{M}(\mathbf{r})$ along its axis but shrinks in the antiparallel case, causing corresponding changes of the overall width of the solitons (Fig. 5). This behavior is natural as the free energy is minimized in the respective cases, consistent with the outcomes of numerical modeling [Figs. 5(c) and 5(d)] [20], as the field prompts expansion of CFLCC regions with $\mathbf{M}(\mathbf{r})\|\mathbf{H}$ and shrinking of regions with $\mathbf{M}(\mathbf{r})$ antiparallel to $\mathbf{H}$.

The observation of magnetic hysteresis curves at $\mathbf{H}\perp\mathbf{n_0}$ [Fig. 1(c)] is due to the localized soliton interior regions having $\mathbf{M}(\mathbf{r})\|\mathbf{n}(\mathbf{r})$ orthogonal to $\mathbf{M_0}$. Beyond these solitons, which are stabilized by the chiral nature of the CFLCCs and the ensuing nontrivial topology [1,5] and can exist at no fields, many long-lived metastable spatial patterns in $\mathbf{M}(\mathbf{r})$ emerge in the confinement-frustrated CFLCCs as a result of magnetic switching, including

periodic stripe patterns (see Fig. S2 in the Supplemental Material [20]) that can persist for hours after the field is turned off. This behavior may be related to the natural tendency of soft matter systems with polar ordering to realize splayed physical fields like $\mathbf{M}(\mathbf{r})$ and can be used in realizing other solitonic configurations, showing a need for developing theoretical foundations for CFLCCs beyond the simple model adopted here [15,20]. These theories may build on studies of solitons in related condensed matter systems of chiral LCs and ferromagnets [1,4,5,7–10], including the modeling of 3D ferromagnetic hopfions [22], albeit CFLCCs differ from both and may enable experimental discovery of isolated $\pi_3(\mathbf{S}^2) = \mathbf{Z}$ solitons. It will be of interest to probe how the topological Hopf index of these $\pi_3(\mathbf{S}^2) = \mathbf{Z}$ solitons can be controlled when they are isolated or appear along with other defects. CFLCCs may also become a model system for understanding knotted field configurations in physical systems beyond condensed matter, ranging from elementary particles to Bose-Einstein condensates and cosmology, in which such knotted fields are studied theoretically, but experimental tests of theoretical models are limited [23–31].

To conclude, we have experimentally realized and numerically modeled 2D skyrmionic and 3D knotted magnetization vector field configurations in a novel soft matter system of CFLCCs. We have demonstrated ferromagnetic switching of such solitons. Although knotted static solitons and torons have been recently controllably and abundantly generated in frustrated chiral LCs in a nonpolar director line field [1,4,5], the knotted configurations demonstrated here are the first such experimental realizations for the magnetization vector field. This work may be extended to obtaining isolated 3D magnetization solitons of different Hopf index and their assemblies into lattices with and without other defects [5]. The experimental platform we have developed may allow for probing the topological transformation of solitonic field configurations driven by weak external stimuli, with potential uses ranging from modeling similar phenomena in other branches of physics, such as particle physics and cosmology [23–31], to applications in magneto-optic devices [32,33].

We acknowledge technical assistance of W. Gannett, M. Keller and Y. Zhang, discussions with A. Bogdanov, A. Fert and A. Hess, and funding from the NSF Grant DMR-1420736.

*Corresponding author.
ivan.smalyukh@colorado.edu

[1] I. I. Smalyukh, Y. Lansac, N. A. Clark, and R. P. Trivedi, Nat. Mater. **9**, 139 (2010).
[2] U. Tkalec, M. Ravnik, S. Čopar, S. Žumer, and I. Muševič, Science **333**, 62 (2011).
[3] A. Martinez, M. Ravnik, B. Lucero, R. Visvanathan, S. Žumer, and I. I. Smalyukh, Nat. Mater. **13**, 258 (2014).
[4] Bryan Gin-ge Chen, P. J. Ackerman, G. P. Alexander, R. D. Kamien, and I. I. Smalyukh, Phys. Rev. Lett. **110**, 237801 (2013).
[5] P. J. Ackerman, J. van de Lagemaat, and I. I. Smalyukh, Nat. Commun. **6**, 6012 (2015).
[6] G. H. Derrick, J. Math. Phys. (N.Y.) **5**, 1252 (1964).
[7] T. H. R. Skyrme, Proc. R. Soc. A **260**, 127 (1961).
[8] M. N. Wilson, A. B. Butenko, A. N. Bogdanov, and T. L. Monchesky, Phys. Rev. B **89**, 094411 (2014).
[9] A. Bogdanov and A. Hubert, J. Magn. Magn. Mater. **138**, 255 (1994).
[10] A. O. Leonov, I. E. Dragunov, U. K. Roßler, and A. N. Bogdanov, Phys. Rev. E **90**, 042502 (2014).
[11] P. J. Ackerman, R. P. Trivedi, B. Senyuk, J. van de Lagemaat, and I. I. Smalyukh, Phys. Rev. E **90**, 012505 (2014).
[12] N. Romming, C. Hanneken, M. Menzel, J. E. Bickel, B. Wolter, K. von Bergmann, A. Kubetzka, and R. Wiesendanger, Science **341**, 636 (2013).
[13] X. Z. Yu, Y. Onose, N. Kanazawa, J. H. Park, J. H. Han, Y. Matsui, N. Nagaosa, and Y. Tokura, Nature (London) **465**, 901 (2010).
[14] A. Fert, V. Cros, and J. Sampaio, Nat. Nanotechnol. **8**, 152 (2013).
[15] A. Mertelj, D. Lisjak, M. Drofenik, and M. Ćopić, Nature (London) **504**, 237 (2013).
[16] H. Hopf, *Selecta Heinz Hopf* (Springer Berlin Heidelberg, 1964).
[17] D. Lisjak and M. Drofenik, Cryst. Growth Des. **12**, 5174 (2012).
[18] R. P. Trivedi, D. Engstrom, and I. I. Smalyukh, J. Opt. **13**, 044001 (2011).
[19] P. Oswald, J. Baudry, and S. Pirkl, Phys. Rep. **337**, 67 (2000).
[20] See Supplemental Material at http://link.aps.org/supplemental/10.1103/PhysRevLett.115.097802 for details about the numerical modeling and relaxation kinetics of stripe patterns in $\mathbf{M}(\mathbf{r})$.
[21] M. N. Wilson, E. A. Karhu, A. S. Quigley, U. K. Roßler, A. B. Butenko, A. N. Bogdanov, M. D. Robertson, and T. L. Monchesky, Phys. Rev. B **86**, 144420 (2012).
[22] A. B. Borisov and F. N. Rybakov, Low Temp. Phys. **36**, 766 (2010).
[23] A. F. Ronada and J. L. Trueba, Nature (London) **383**, 32 (1996).
[24] Y. Kawaguchi, M. Nitta, and M. Ueda, Phys. Rev. Lett. **100**, 180403 (2008).
[25] Y. K. Liu, C. Zhang, and S. J. Yang, Phys. Lett. A **377**, 3300 (2013).
[26] N. R. Cooper, Phys. Rev. Lett. **82**, 1554 (1999).
[27] P. Sutcliffe, Phys. Rev. B **76**, 184439 (2007).
[28] S. Bolognesi and M. Shifman, Phys. Rev. D **75**, 065020 (2007).
[29] A. Gorsky, M. Shifman, and A. Yung, Phys. Rev. D **88**, 045026 (2013).
[30] A. Acusa, E. Norvaišasa, and Ya. Shnir, Phys. Lett. B **733**, 15 (2014).
[31] A. Thompson, A. Wickes, J. Swearngin, and D. Bouwmeester, J. Phys. A **48**, 205202 (2015).
[32] A. Mertelj, N. Osterman, D. Lisjak, and M. Ćopić, Soft Matter **10**, 9065 (2014).
[33] A. J. Hess, Q. Liu, and I. I. Smalyukh, Appl. Phys. Lett. **107**, 071906 (2015).